Towards reliable oxidation state analysis of tin halide perovskites with XPS

Amanz Azaden[a], Prajna Bhatt[b], Yuhan Liu[b], Jiewen Wei[a], Saif A. Haque[a]*, Robert G. Palgrave[b]*

a. Department of Chemistry and Centre for Processable Electronics, Molecular Sciences Research Hub, Imperial College London, London W12 0BZ, U.K.

b. Department of Chemistry, University College London, 20 Gordon St, London WC1H 0AJ

*corresponding authors: r.palgrave@ucl.ac.uk, s.a.haque@imperial.ac.uk

Abstract

Tin is the most promising replacement for lead in hybrid halide perovskite solar absorbers. A disadvantage of tin perovskites is ease of oxidation of Sn(II) hampering optoelectronic performance and long-term stability. Quantification of the extent of Sn oxidation in hybrid halide perovskites is therefore an important indicator of material stability but remains a significant challenge. X-ray photoemission spectroscopy (XPS) is commonly used to measure Sn chemical environments; we show here that conventional approaches to fitting the Sn 3d spectra from perovskite surfaces can easily lead to erroneous conclusions about the tin oxidation state. We consider several approaches to developing a robust fitting model for Sn 3d spectra. Furthermore, we identify that tin halide perovskite surfaces can be unstable under XPS measurement conditions, and the chemical state of tin will change significantly over typical analysis times. We use correlation analysis to validate our fitting model and identify phases present.

Introduction

X-ray photoelectron spectroscopy (XPS) is one of the most widely used surface analysis techniques, and has become particularly important in analysis of metal halide perovskites.[1] This class of materials has been of intense interest for over a decade because of potential applications as photovoltaic absorbers, rivalling well established technologies owing to their remarkable optoelectronic properties, facile processing routes and commercially-relevant PCEs.[2] An important focus of current perovskite research is the substitution of lead for less toxic tin.[3] Sn(II) has a $5s^2$ valence electron configuration, analogous to the $6s^2$ configuration of Pb(II).[4] Tin based perovskites typically display narrower band gaps and may avoid the need for encapsulation, which is necessary for Pb-based perovskites.[5]

Sn based perovskites have shown a significant increase in photovoltaic efficiency in the past decade, but one of the key challenges is control of oxidation state. Sn(II) is more susceptible to oxidation than Pb(II), as the valence electrons of Sn experience lower effective nuclear charge than those of its heavier congener. In addition to the energetic driving force for this oxidation, Lanzetta *et al.* demonstrated the significance of I_2 generation in Sn-PSCs, which leads to a cyclic degradation with detrimental self-doping resulting in a p-type perovskite layer.[6] These fundamental studies of the degradation of the active layer have thus far proved useful in designing a road map for mitigating oxidation. Use of additives and compositional engineering is a common strategy to inhibit Sn oxidation in PSCs.[7-10] For example, addition of small amounts of SnF_2, Sn metal and NH_4SCN which can act as reducing agents without fundamentally changing the perovskite morphology. Moreover, the incorporation of bulky 2D cations in the A site of the ABX_3 structure have been shown to aid highly-oriented crystallisation in addition to inhibiting oxygen ingress and Sn oxidation. Understanding how different additives and synthetic procedures affect Sn oxidation requires a

https://doi.org/10.26434/chemrxiv-2024-zmn02 **ORCID:** https://orcid.org/0000-0003-4522-2486 Content not peer-reviewed by ChemRxiv.

reliable measure of the Sn oxidation state. Since oxidation of the perovskite films is often a surface process, XPS has emerged as the main technique for understanding Sn-PSC oxidation chemistry.

As a surface technique capable of distinguishing different oxidation states or chemical environments of the same element, XPS is well suited for studying perovskite films. In XPS, different chemical environments may appear at different binding energies, known as the chemical shift, due to changes in the energies of initial and final states.[11] However, XPS often produces spectra where chemical environments are not completely resolved; when peak width exceeds the peak separation then peak fitting is required to determine the concentration ratio of the two chemical states. For the tin perovskites, a key aim is to quantify the amount of Sn(II) compared to the Sn(IV). The chemical shift between Sn(II) and Sn(IV) has been a controversial topic in XPS. For the tin oxides, it has been concluded by some that the core lines do not offer definitive distinction between SnO and SnO_2, but instead the valence band region or Auger-Meitner peaks should be used.[12, 13] For the tin sulfides, a chemical shift of around 0.5 eV is apparent in the core lines.[14] For the halides, typically it is asserted that a chemical shift of around 0.8 eV is apparent between Sn(II) and Sn(IV). However, even a chemical shift of this size will require modelling of the spectra to extract the relative size of each component. In building such a peak model, many parameters must be specified, and different choices can lead to markedly different values of the Sn(II):Sn(IV) ratio determined from the same experimental data. There are many examples in literature where the outcome of the XPS model is essential to the conclusions of the paper, but no details are given of how the model is constructed or constrained.[15] We show here that these choices have profound effect on the conclusions on Sn chemical environment.

Li et al. recently pointed out misuse of XPS in the Pb-based perovskites.[16] Since XPS is often the only technique used to assess the Sn oxidation state in perovskite thin films, it is equally important that XPS is interpreted correctly when studying Sn-based perovskites. Without robust models to determine Sn(II):Sn(IV) ratio, misleading conclusions on the efficacy of certain additives, or the relationship between Sn oxidation and device performance can be made. Here we present detailed XPS investigations on Sn halide perovskite films, based upon parameter selections in the model. We highlight that very common practices in both measurement and data analysis may give rise to misleading conclusions and consequently undermine the results of many studies in this field. We describe what we consider to be a more robust experimental design and make suggestions for future investigations.

Results

XPS was carried out on thin films of perovskites deposited via conventional device fabrication methodology of the tin perovskite field, see Experimental Methods for full details. We first describe the appearance of the surface of a film with nominal composition $PEA_{0.2}FA_{0.8}\,Sn(I_{0.9}Br_{0.1})_3$ under XPS analysis. As per the experimental section, film fabrication was undertaken in a nitrogen filled glovebox with O_2 level below 0.5ppm. XPS analysis was subsequently undertaken by transferring these films to the spectrometer via one of two methods;

Through air transfer: films contained in glass vials were vacuum sealed in the fabrication glovebox and transported to the spectrometer, before removal in air and rapid transfer onto the sample stage, pumping down to below 1 mbar in under three minutes.

Inert transfer: sealed samples from the fabrication glovebox were transferred to an inert 0.1ppm> N_2 glovebox and mounting the samples on an inert sample holder prior to spectrometer loading.

Spectra obtained from both sample preparation routes yielded an XPS survey containing the elements Sn, C, N, I, Br, O on the surface. The surveys and principle corelines are shown in Figure 1.

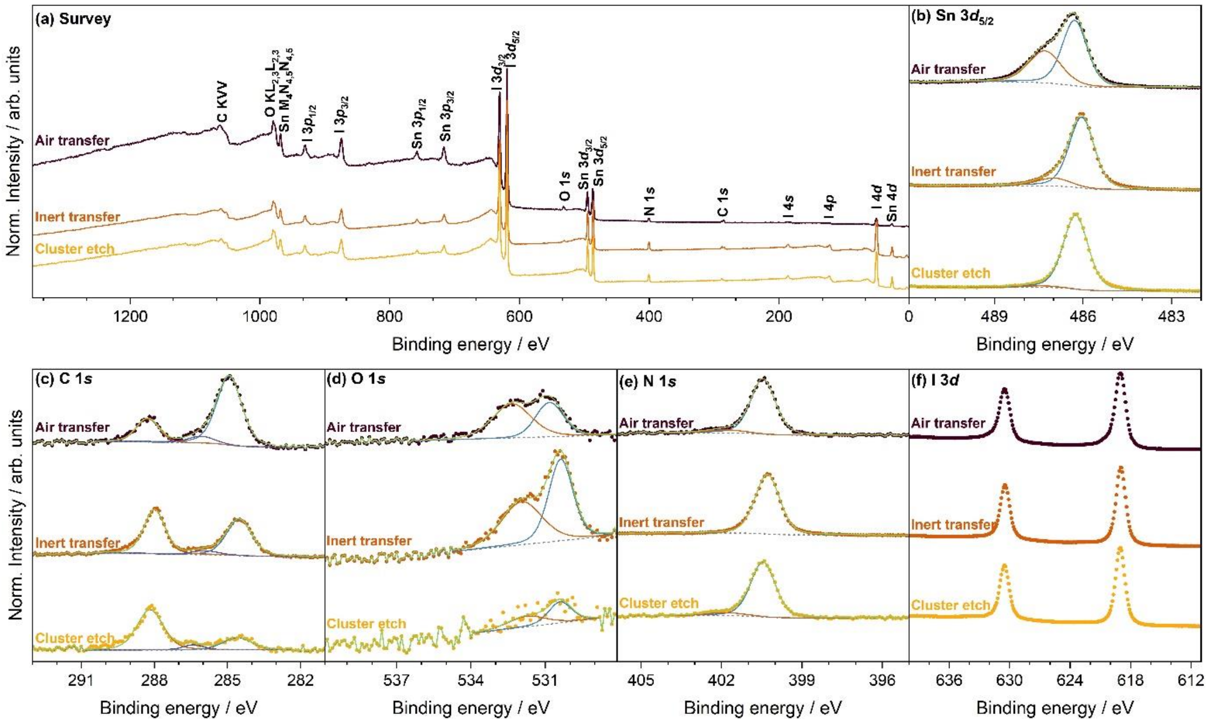

Figure 1. Survey (a) and core level spectra (b-f) from tin perovskite films, introduced into the spectrometer though air or vis inert transfer. Spectra from the cluster etched inert transfer sample are also shown.

Before discussing the fitting of the core line spectra, we address the charge correction. Charging in XPS occurs due to creation of a surface potential which changes the measured binding energy values.[17] A typical procedure to correct for this is to use an internal standard: a core line with a known binding energy. C 1*s* from adventitious carbon is often used for this despite well known drawbacks.[18, 19] In this case we choose to correct the BE scale to the I 3d arising from the iodide in the perovskite phase. The rationale for this choice is that the iodide environment is likely to be the only iodine environment present in high concentration so is easy to identify unambiguously, it belongs to the majority phase of the sample so charging affecting this peak should affect the majority phase the same way, and the C 1*s* peak is a poor choice in this case as it contains contribution from not only adventitious carbon but also FA and PEA derived carbon. We set the I 3*d* peak to 619.0 eV, and all other peaks are relative to this value.

Fitting of Sn 3d peak

A typical Sn 3d spectrum for a $PEA_{0.2}$ $FA_{0.8}$ $Sn(I_{0.9}Br_{0.1})_3$ perovskite is shown in Figure 1. Determining the [Sn(II)]:[Sn] ratio (the proportion of the total Sn that is Sn(II)) is usually accomplished by fitting the Sn 3$d_{5/2}$ peak with two components, or sometimes three components,[20] the third representing Sn(0).[21] Given the critical nature of this fitting and its conclusions to studies on the stability of Sn perovskites, we will demonstrate the importance of different Sn 3*d* fitting approaches.

We focus here specifically on the Sn 3$d_{5/2}$ peak shown in Figure 2 which is taken from a perovskite film measured via *inert transfer* to minimise surface oxidation. Despite minimal exposure to air the Sn 3$d_{5/2}$ peak is clearly asymmetric and characteristic of two or more components. We fit the peak as follows: two components are used in the model, and we label these Sn(A), which is the lower binding energy component usually assigned as Sn(II), and Sn(B), which is the higher binding energy component usually (but not always) assigned as Sn(IV). Both A and B components are modelled as a pseudo-Voigt line shape (a sum of Gaussian and Lorentzian line shapes) with 30% Lorentzian and 70% Gaussian weighting. This is implemented as the SGL(30) line shape in CasaXPS. If this model is fitted without constraints on FWHM, position or intensity of either component, a result which matches the experimental spectrum very well is obtained. Both linear and Shirley backgrounds were tiraled, with limits chosen to be on reasonably flat parts of the spectrum either side of the Sn $3d_{5/2}$ peak. Table 1 shows the results of these mathematical best fits (Models I and II). The Sn 3*d*(A) percentage was significantly different depending on what background was chosen (51% for linear and 60% for Shirley). Given the ubiquity of Shirley background usage, we proceed from here using that background alone, but note that background type is clearly an important choice for this fitting and should be specified and kept constant within a single programme of analysis.

Even with identical background functions, it is noted that it is quite possible that a large range of models might fit the experimental data with almost equal goodness of fit. To illustrate the relationship between fitting and the corresponding [Sn(A)]/[Sn] ratio, we manually constrained this composition ratio at regular intervals. At each defined ratio, the values of the FWHM of both the Sn(A) and Sn(B) components that gave the best fit were plotted with the corresponding residual standard deviation (RSD): a measure of the goodness of fit, where smaller values indicate a better fit. These values were obtained by allowing the FWHM and BE positions of the components to vary. The results are shown in Figure 1. The RSD has a minimum at 2.47 for 59.8% Sn(A), making this the mathematically best fit. However, every fitting between 25-65% Sn has a RSD value below 4. For context, fitting a single component gives a RSD of 12.56. Visually, fits from 30-65% Sn(A) all match very well to the experimental data, and for this dataset a very wide range of Sn(A) concentrations can be obtained from a simple, unconstrained two component fit with almost equal goodness of fit. Thus, although c. 60% Sn(A) is identified as the best mathematical fit, the confidence level in this as an analytical result must be low, as such a wide range of compositions could also be obtained with only a small increase in RSD. This issue is not unique to this dataset by any means. In fact, it is our view that the majority of Sn 3*d* datasets from halide perovskites in the literature we have examined suffer from the same issue. Thus, our first conclusion is that choosing the mathematical best fit, or indeed choosing a fit that looks visually acceptable, may be insufficient to ensure reliable conclusions; if meaningful Sn oxidation state concentrations are to be obtained from XPS, then additional information must be included in the model.

Sn 3d Fitting - Equal FWHM Model

We now consider several approaches to building a robust model for the [Sn(A)]:[Sn] ratio.

A simple form of constraint that is commonly applied is to set the FWHM of separate components equal to each other. Core line width in XPS is determined mainly by core-hole lifetime, vibrational broadening, charging, X-ray linewidth and spectrometer energy resolution.[22] For many samples it may be reasonable to assume FWHM of components of the same core-line are equal - this can be helpful in preventing unphysical models with some components very wide and others very narrow, although there are many examples of practical situations where an equal FWHM model is not a suitable fit – organic polymers is a classic example where differing vibrational broadening changes the width of some core-line components.[23] Constraining the two Sn components to be of equal FWHM in the model described above, would lead to a result of 69.3% Sn(A), with both component having a FWHM of 1.08 eV. This gives a Sn(A) concentration significantly greater than the mathematical best fit.

Table 1. Summary of models for fitting of Sn $3d_{5/2}$ peak. In each case the background is fixed as Shirley unless noted, two components are used with peak shapes fixed as a 30% Lorentzian 70% Gaussian sum. FWHM and binding energy are allowed to vary, shaded boxes indicate constraints applied.

	Model Name	BE / eV Corrected to I $3d_{5/2}$ at 619.0 eV		FWHM / eV		[Sn(A)] /[Sn]
		Sn(A) component	Sn(B) component	Sn(A) component	Sn(B) component	
I	Mathematical best fit *Linear background*	486.20	487.13	0.94	1.42	51.4%
II	Mathematical best fit	486.20	487.23	1.00	1.27	59.8%
III	Equal FWHM	485.78	487.33	1.08	1.08	69.3%
IV	Sn(II) standard $CsSnI_3$ nanocrystals	485.71	486.68	0.98	1.29	58.0%
V	Sn(IV) standard Cs_2SnI_6	485.72	486.68	0.99	1.30	58.4%
VI	Sn(IV) standard SnO_2	485.70	486.64	0.98	1.39	54.9%

Sn 3d fitting - Use of standard spectra to constrain FWHM

Comparison of an analyte with a known standard is perhaps one of the oldest analytical methods known and is particularly useful in XPS analysis. We consider the use of standard spectra to fix the FWHM for the Sn $3d_{5/2}$ peaks in perovskites. A drawback of this approach is that the FWHM is contributed to by charging, and there is no guarantee the same material will charge in the same way in our pure standard compared with the more complex perovskite surface. However, this does provide a way to infer which components will have a greater FWHM and we use it here with the stated drawbacks in mind.

If Sn(A) and Sn(B) are considered to be Sn(II) and Sn(IV) respectively, this can be done by considering a chemical standard for the Sn(II) or the Sn(IV).

If the Sn(IV) is to be considered a halide, then a possible class of standard compounds representing Sn(IV) is the A_2SnX_6 compounds, so-called vacancy ordered double perovskites which benefit from being reasonably air stable, containing nominally only Sn(IV) and being unlikely to contain Sn(II), as reduction of Sn(IV) is unfavourable under the synthetic and storage conditions typically used. We have previously measured XPS spectra of A_2SnX_6 compounds and have reproduced and remeasured a sample of Cs_2SnI_6 for use as a standard here. We find the Sn $3d_{5/2}$ peak from Cs_2SnI_6 to be symmetric with a FWHM of 1.30 eV. Alternatively, the Sn(IV) might be considered an oxide, in this case SnO_2 is the best standard. We measure a commercial SnO_2 powder and find a FWHM of the Sn $3d_{5/2}$ peak of 1.39 eV.

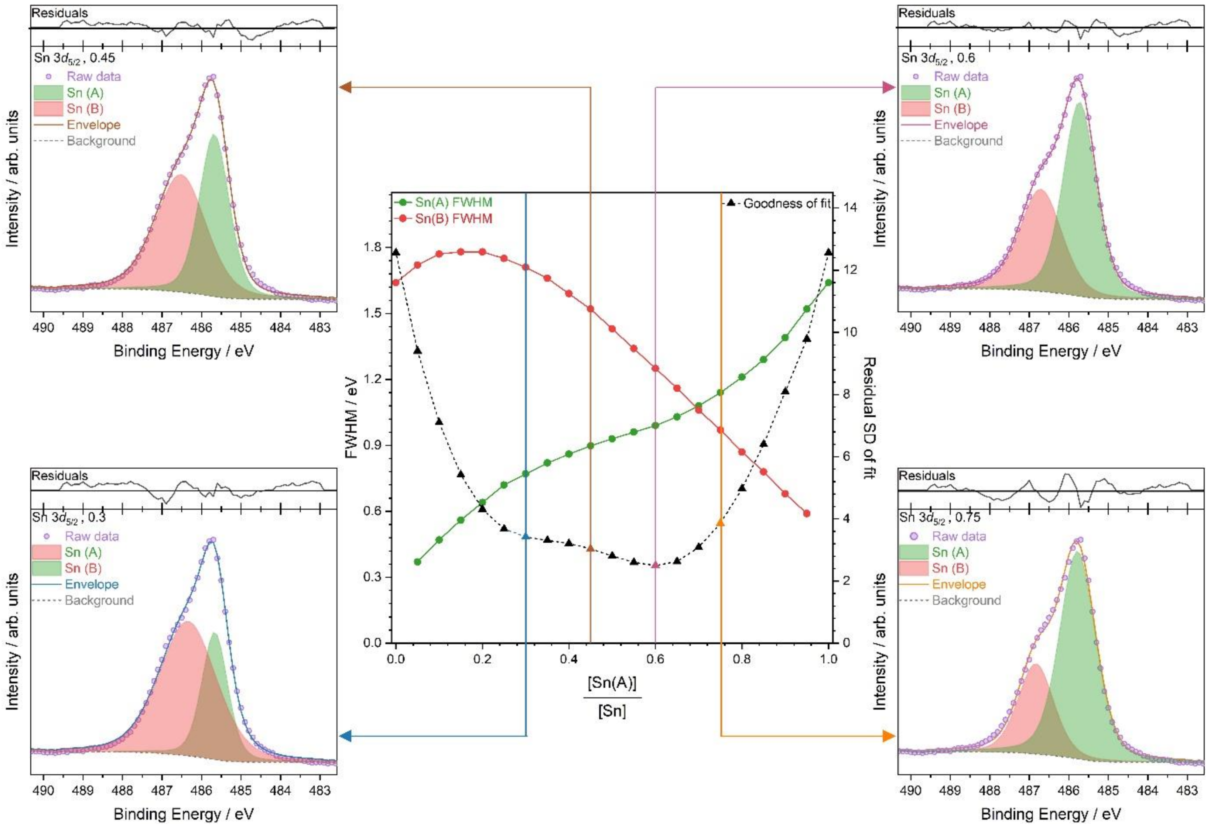

Figure 2. Comparison of models of the Sn 3d peak for an air-exposed tin perovskite. The same spectral data is fitted with different two-component models, where Sn(A) is the low binding energy component and Sn(B) the high binding energy component. Peak shape and background were identical in each fit. The FWHM and component positions were allowed to vary, and the best fit calculated for [Sn(A)]/[Sn] ratios between 0 and 1. The goodness of fit is shown as black points in the central graph, and the corresponding FWHM of each component is shown as green and red points for Sn(A) and Sn(B) respectively. Example fittings for four different values of [Sn(A)]/[Sn] are shown. For each fitted spectrum, the residual to the fit is shown above the spectrum.

Obtaining a pure standard for Sn(II) is more difficult owing to rapid oxidation of Sn(II) compounds which occurs first at the surface. We look to $CsSnI_3$ nanocrystals capped with oleate ligands which inhibit oxygen ingress and subsequent oxidation. We analysed a sample of such nanocrystals produced as described in the Experimental Section. The Sn $3d_{5/2}$ peak was symmetrical, with a FWHM of 0.98 eV. We can use these FWHM values to fit the Sn 3*d* peak from our perovskite film.

We contrast these approaches in Table 1*,* using these standards on our perovskite film surface. Encouragingly, fits using either one of the standard FWHM values for Sn(A) or Sn(B) causes the other FWHM to be very close to the opposite standard. In model IV, when the Sn(A) standard FWHM of 0.98eV is used, and the Sn(B) FWHM allowed to vary, a value of 1.29eV for the Sn(IV) FWHM is produced by the fitting procedure. This is almost identical to the standard FWHM from Cs_2SnI_6 (1.30 eV). Similarly, in model V, Table 1, constraint of the Sn(B) to 1.30eV or 1.39 eV yields a value for Sn(A) FWHM almost exactly the same as that seen in the $CsSnI_3$ standard. Both these models agree on the Sn(A) level at 58% to two significant figures – a slightly lower level of Sn(A) than the mathematical best fit for the Shirley background.

Given the consistency of peak models IV and V, we will take the FWHM of these standards forwards, and consider their accuracy when used in a variety of different situations as described below, although as discussed below, our final conclusions on the identity of Sn(A) and Sn(B) do not exactly align with the assumptions made in producing the model. We now proceed with the full description of the chemistry of the sample surfaces.

Perovskite film analysis: surface and depth profiling

Survey and core line spectra for the through-air and inert-transfer samples are shown in Figure 1. The inert transfer-sample was etched using cluster ions and spectra from the etched surface are also shown in Figure 1, and discussed in more detail below. For the N 1*s*, O 1*s* and C 1*s* corelines, we carried out a simple two or three-component fit, where two pseudo-Voigt lineshapes were fitted to the spectrum without constraint on FWHM or position. The N 1*s*, coreline appeared narrow and symmetrical in all cases with typical FWHM of 1.2 eV and binding energy of 400.3 eV, except the through-air transfer sample, where an asymmetric peak was seen, with a smaller component, representing about 8% of the N 1*s*, signal, and located 1.4 eV above the main N 1*s*, peak. The C 1*s* coreline consisted of two maxima and was fitted well with a three-component model. C 1*s* components were found at around 284.6 eV and 288.0 eV, with a smaller component at around 286.2 eV binding energy, this last component representing less than 10% of the C 1*s* signal. The O 1*s* signal was fitted with a two-component model, with a narrow component with typical FWHM of 1.2 eV, at a binding energy of 530.2 eV, and a broader component, typical FWHM of 2.5 eV, at a binding energy of 532.1 eV. The larger breadth of this latter peak is suggestive of a hydroxide or organic environment.

The nominal perovskite composition, $PEA_{0.2}FA_{0.8}Sn(I_{0.9}Br_{0.1})_3$ (excluding hydrogen atoms which are not detected by core line XPS) is 12.5 $\%_{at}$ Sn, 30 $\%_{at}$ C, 12.5 $\%_{at}$ N and 37.5 $\%_{at}$ anion (iodide and bromide combined). The carbon from the FA cation is assumed to be represented by the C 1*s* component at 288.0 eV, and that from the PEA is assumed to be at 285 eV, in accordance with assignments from literature.[24] Figure 3 and Table 2 shows the relative proportions of the elements found in each of the samples, determined by measuring the peak areas of the principal core lines (Sn 3*d*, C 1*s*, O 1*s*, Br 3*d*, I 3*d*).

The *through air* sample contained a significant amount of oxygen (8.9 $\%_{at}$) and non-FA carbon (19.4 $\%_{at}$). The anion:Sn ratio was just over 4:1, much higher than the nominal value of 3:1, meaning that significant amounts of anion were not associated with Sn, or that Sn had been oxidised and was bound to a greater amount of anion than expected. Analysis of the Sn 3d peak as described above suggested 61% of the Sn was Sn(A), commonly assigned as Sn(II) , and 39% was Sn(B), commonly assigned as Sn(IV).

The *inert transfer* sample, in contrast, has a lower amount of oxygen (4.9 $\%_{at}$). Non-FA carbon concentration (*i.e.* all carbon apart from the 288 eV environment) is similar to the through air sample, suggesting that this contamination is picked up during synthesis and subsequent handling, rather than during transfer through air. The anion:Sn ratio is 3.4:1, closer to the nominal ratio than the through air transfer sample. The Sn(A) percentage was 87%, and 13% was Sn(B), commonly assigned as Sn(IV). The inert transfer sample is reasonably close to the nominal value for $PEA_{0.2}FA_{0.8}Sn(I_{0.9}Br_{0.1})_3$ (Table 2)

The inert transfer sample was then etched with Ar^+ cluster ions. Here we use a cluster size of 3000 Ar ions. The composition was measured at intervals during the etching progress, and the compositional depth profile is shown in Figure 3. Etching removed much of the C 1*s* 284.6 eV environment, as well as lowering the oxygen and Sn(B) concentrations. The concentrations of iodine, nitrogen, C 1*s* 288eV environment (corresponding to FA) and Sn(A), interpreted as Sn(II), approached their nominal values for an $FASnI_3$ (Figure 3, Table 2). After around 500 s of cluster etching, the concentrations of N and C 1*s* 288eV began to gradually fall. This may indicate that extended etching, even with cluster ions, preferentially removes the FA^+ ion, leaving a tin and iodine rich surface. The C 1*s* environment at 284.6 eV remains into the bulk of the film, persisting at around 5 $\%_{at}$. This may represent the presence of PEA^+ in the bulk, bulk contamination with a graphitic like carbon species, or it may be the result of FA^+ degradation into such a species, although FA^+ in the presence of iodide is thought to typically decompose into HCN, NH_3, formamidine and HI all of which would be expected to escape into the vacuum under these experimental conditions.[25] Note the N:C(288eV) ratio remained very close to the nominal value for FA^+ cation throughout the etching, suggesting that the FA^+ cation is etched from the surface as a unit, or if the FA^+ does decompose, the carbon must be transformed into a different chemical environment, and the nitrogen must be removed from the surface. Two oxygen environments were observed, at c. 530 eV and 532 eV, referred to as O(A) and O(B) respectively. Oxygen levels decreased during by cluster etching to around 1 $\%_{at}$ total oxygen level, suggesting the concentration in the bulk of the film is very low, or that the oxygen is preferentially removed by the sputtering process.

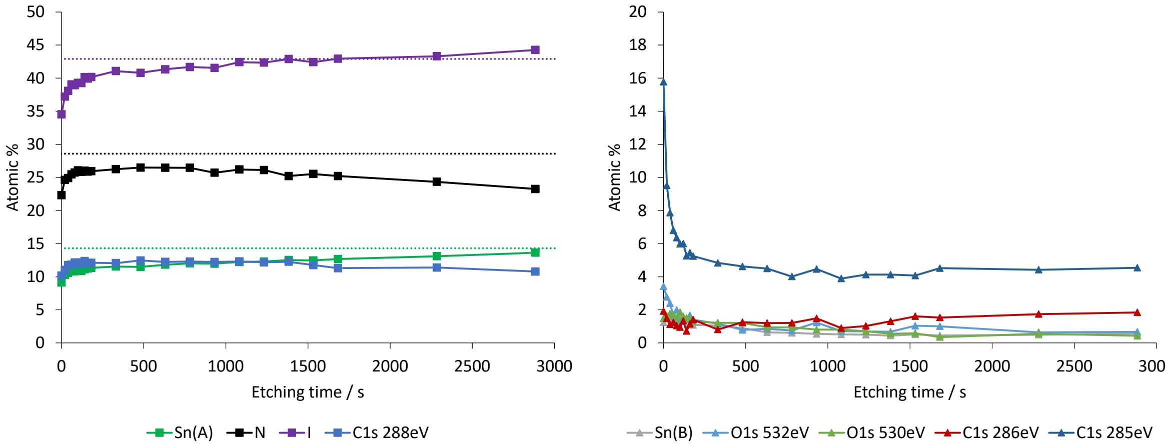

Figure 3. Cluster etching depth profile of a tin perovskite film. Horizontal lines show the nominal concentrations of each element or chemical environment. The Sn(A) and Sn(B) are typically interpreted as Sn(II) and Sn(IV). Left panel shows the expected components of the film, right panel shows additional detected elements and components.

After *c*. 1500s of etching, the sample was closest to the nominal composition. The anion:Sn ratio was 3.2:1, and the Sn(A) percentage was 96%. Beyond this point, the N and C1s (288 eV) content fell slightly, likely due to preferential removal of the FA^+ cation during prolonged etching. Above 1500s etching, a low binding energy N 1*s* environment emerged around 398.3 eV, reaching around 8 $\%_{at}$ of the Nitrogen present by 2800 s etching, perhaps indicating some decomposition of the FA^+ into non-volatile products, this could be a triazine species as observed in thermal FA^+ degradation by Juarez-Perez *et al*.[25] The total amount of N and C decrease at long etching times, while Sn and halide concentration increase, which may indicate transformation towards a SnX_2 like surface.

Together these results indicate that the as-presented samples, even introduced through inert transfer, have surface contamination of carbon, oxygen and Sn(B) and that the anion to metal ratio is high. Oxygen levels and anion:metal ratio were higher in the through air transfer compared to the inert transfer, indicating oxidation and/or contamination of the surface occurs by air exposure, even for approximately 3 minutes. Etching with cluster ions removes most of the oxygen and non-FA carbon and leaves a surface with composition with very low Sn(B) concentration, and close to nominal ABX_3 overall composition.

We note that synthesis method has a very large impact on the degree of oxidation and surface contamination in these samples. Careful control of synthesis process must be achieved to obtain reproducible surface compositions.

Table 2. Compositions in atomic% found experimentally, and according to the nominal perovskite formula.

	Through air	*Inert Transfer*	*Inert Transfer, cluster etch 1500 s*	*Nominal* $PEA_{0.2}FA_{0.8}Sn(I_{0.9}Br_{0.1})_3$	*Nominal* $FASnI_3$
Sn (total)	9.5	10.1	13.8	12.5	14.3
Sn(A) (low BE)	*60.8%*	*86.8%*	*97.2%*	*100%*	*100%*
Sn(B) (high BE)	*39.2%*	*13.2%*	*2.8%*	*0%*	*0%*
O 1*s* (A) c. 530.1 eV	4.7	1.50	0.41	-	-
O 1*s* (B) c. 532.2 eV	4.9	3.4	0.69	-	-
N 1*s*	17.8	22.5	23.2	20	28.6
(I + Br)	38.6	34.7	44.2	37.5	42.9
C 1*s* (288.0 eV, FA)	5.3	10.2	11.7	10	14.3
C 1*s* (286.2 eV)	3.9	1.9	1.37	-	-
C 1*s* (284.6 eV)	15.3	15.8	4.70	20	-
(I + Br) : Sn	4.1	3.4	3.2	3	3
N : C (FA)	3.4	2.2	2.0	2	2

Stability of the perovskite surface under XPS conditions

The stability of the air exposed tin perovskite surface under XPS measurement conditions was studied. It is known that Pb based perovskites suffer from surface damage in ultrahigh vacuum conditions,[26] and Gupta *et al*. previously reported that in Sn based perovskites, reduction could occur under XPS conditions.[27] Here we further explored this phenomenon. Partially oxidised tin perovskite surfaces were exposed to either X-rays + dual beam flood gun or X-rays alone. The sample exposed to only X-rays showed a slight increase in the proportion of Sn(A), moving from 61.1% Sn(A) to 64.1% Sn(A) after 30 minutes of X-ray exposure. When the dual beam flood gun was used, the effect was greater: in 30 minutes the surface Sn(A) component rose from 65.5% before exposure to 74.4% after exposure (Table 3). In both cases, the increase in the Sn(A) porportion was associated with removal of oxygen from the surface.

Table 3. Changes to the sample surface on exposure to XPS conditions.

	[Sn3d(A)]/[Sn]		Oxygen atomic %	
	Before exposure	After 30min exposure	Before exposure	After 30min exposure
X-rays only	61.1%	64.1%	11.0%	6.1%
X-rays + Ar^+ dual beam flood gun	65.5%	74.4%	8.3%	3.6%

To further study the stability of the surface under measurement conditions, a new, partially oxidised sample was analysed. The following protocol was used. Scans of Sn 3*d*, O 1*s*, I 3*d* were repeatedly recorded for a period of 50 minutes. Each set of scans took approximately 1 minute to collect, providing 50 iterations of measurements with around 1 minute time resolution. The intention of this protocol is to achieve high time resolution, so only I 3*d*, O 1s and Sn 3*d* high resolution scans were undertaken. Thus in these scans, total $\%_{at}$ cannot be measured as has been done above, as C, N corelines were not measured, rather the aim is to understand relative compositional and chemical changes in those elements measured. The initial spectra appeared similar to those reported above for partially oxidised perovskite surfaces (Figure 4a,b,c). This surface had an initial [Sn(A)]/[Sn] of 57.5%, typical of air exposed surfaces discussed above. Figure 4d shows the compositional changes on exposure to X-ray + flood gun. The Sn 3*d* and O 1*s* regions were fitted as described above. The overall composition change is seen in Figure 4d; the O 1*s* (B) content decreases immediately from the start of the iteration. The Sn(B) (the higher binding energy component) remains roughly constant for around 5 mins, then begins to decrease. Not plotted in Figure 4d is the O 1*s* (A) concentration which is almost completely coincident with the Sn(B), the implications of this will be discussed below.

In addition to changes in composition, peak binding energy positions also changed with X-ray + flood gun irradiation time. Figure 4e shows the shift in binding energy of each of the core lines and components considered in this analysis compared with their positions at the first iteration. The I $3d_{5/2}$ peak shifted to higher absolute binding energy; on the first iteration, the I $3d_{5/2}$ peak was at 618.51 eV; it shifted to 618.95 eV after 50 minutes of exposure, a shift of +0.44 eV. The shape of the I 3*d* peak did not change, nor did the FWHM increase. As with the iodide core line, the Sn(II) component of the Sn 3*d* peak also shifted to higher binding energies by almost exactly the same amount as the I $3d_{5/2}$, moving from 485.71 eV to 486.17 eV, a total change of +0.46eV.

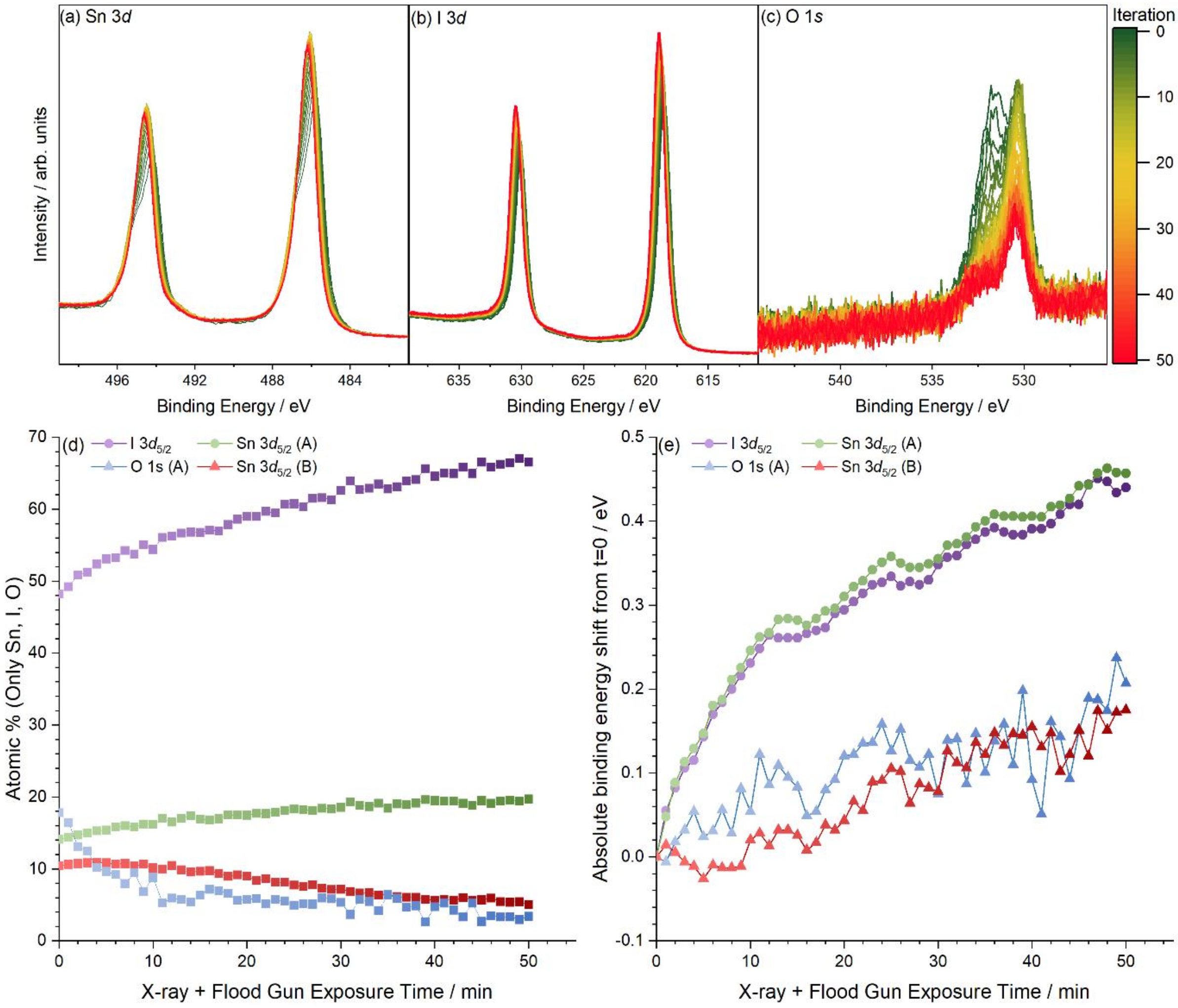

Figure 4. Effects on the surface of a partially oxidised Sn perovskite upon beam damage over time. Spectra are not charge corrected, raw experimental BEs are used here. Panels (a,b,c): spectra taken at approximately 1 min intervals upon exposure to XPS conditions (X-rays + Flood Gun). Changes are shown in composition (d) and binding energy (e) of components indicated with exposure time. NB atomic % values only contain Sn, I and O, as other corelines were not measured in this experiment, see text for discussion. In panel (e), binding energy shift for each coreline is measured from the value at the first iteration.

To further examine the relationship between the different corelines in this 50 spectrum dataset, we employ the concept of correlation analysis in photoemission spectroscopy (Figure 5).[28] We consider the possible relationships between the I 3$d_{5/2}$, O 1*s*(A) O 1*s*(B) Sn(A) and Sn(B) by plotting each of their $\%_{at}$ values against each other – these 10 pairwise correlations plots are shown in the top and left of Figure 5. In the bottom and right of the same figure is shown the pairwise correlation plots of the binding energies of the corelines. In correlation plots of the atomic composition, a straight line represents a constant ratio of the chemical environments across all datasets. This would be expected if the two chemical environments are present in the same phase which retains its overall composition across the dataset. The gradient of the line represents the ratio of one element to the other, which is the stoichiometry of the phase. For example, if the phase $FASnI_3$ is present, and is the only phase to contain I and Sn(A), we would expect the I and Sn(A) to be linearly correlated with a gradient of 1:3, and an intercept of zero. A negative correlation, or non-linear correlation between two elements can mean that they are not in the same phase, but see Bhatt *et al* for a full discussion of this point.[28]

Turning to the BE correlation plots, we must consider the causes of BE changes in XPS. Chemical changes are the most widely used interpretation of binding energy changes. However, it is important to note that the binding energy scale in XPS is referenced to the Fermi Level, so core lines of a particular element will be affected by changes to the Fermi level in the phase that the element belongs to. A positive shift in binding energy occurs if a material becomes more n-type; as the Fermi Level rises, it moves further from each core level. If multiple phases are present within the analysis volume, these phases may not necessarily be in electrical contact, for example if they are poorly conducting, or separated by an insulating boundary layer. In such a case it is possible that Fermi levels are not equal between different phases. In our present dataset, the shape and width of the peaks are almost completely unchanged across all 50 iterations. Because of this we proceed with this analysis using the assumption that the elements we studied are not changing chemically during this process, and instead the binding energy shifts that we observe are due to a change in the Fermi level of their respective phases.

In BE correlation plots, chemical environments belonging to the same phase will undergo the same Fermi level shifts, so their binding energies should correlate linearly across the dataset with a gradient of 1. Non-linear, negatively, or linear correlations with gradients very different to 1 are likely to arise from pairs of chemical environments that are not in the same phase, or from instances where one or both chemical environments are undergoing significant chemical changes.

We can now examine the correlation plots seen in Figure 5. First considering the composition correlations shown in the top left half of the figure. The majority of pairs of corelines give negative correlations (a, b, c, e, f, g). Two pairs give non-linear correlations (i and m). Only panels d and j show linear correlations with positive gradients. These correlations belong to I 3$d_{5/2}$ with Sn(A), and Sn(B) with O 1s(A). I 3$d_{5/2}$ and Sn(A) are strongly linearly correlated, with a gradient of 3.25. The expected gradient of the phase, or phase fraction of $FASnI_3$ is 3. The slightly greater gradient means that the actual composition is more iodine rich than expected from the perovskite formula, and may indicate the presence of some Sn vacancies or oxidised Sn within the perovskite. The intercept represents the amount of one element that would remain if the other element were at zero concentration. In this case the intercept is 2.1 $\%_{at}$ Iodine, indicating that this amount of iodine is present outside of the $FASnI_3$ phase.

The correlation between the $\%_{at}$ of Sn(B) and O 1s(A) is also linear, with a gradient of 0.99, and an intercept of almost exactly zero. The correlation between the $\%_{at}$ of Sn(B) and O 1s(A) is also linear, with a gradient of 0.87, and an intercept of 0.99 $\%_{at}$ Sn. This would correspond to a phase containing Sn 3d(B) and O 1s(A) in almost equal amounts, with a small amount of Sn(B) left over outside of that phase.

In the lower right half of Figure 5 we plot the correlations between binding energies of the stated components. As argued above, if two elements exist in a single phase and do not undergo any chemical changes across the dataset, their BE difference should be constant, and the correlation plot would be linear with gradient of one. This is what is observed for the Sn(A) and I 3$d_{5/2}$ correlation plot (panel h, Figure 5), where the gradient is 1.03 and a goodness of fit R^2=0.99. Together with the correlation between the $\%_{at}$ of these two chemical species, we conclude that Sn(A) and iodine are together in a phase with close to 1:3 composition (we conclude this is the perovskite phase) and that neither Sn(A) nor iodine exists in significant quantity in another phase in this sample. Our conclusion is as above, that the Sn(A) environment corresponds to Sn(II). This conclusion also supports the modelling of the Sn 3$d_{5/2}$ peak described above, as the realistic behaviour of the model across 50 datasets, not only in providing good fits to each Sn 3d spectrum, but also the expected $\%_{at}$ and binding energy correlations, is strongly indicative that our core line model for the Sn 3d is accurate.

Several other BE correlations appear linear in figure 5. Most clearly, the O 1*s*(A) and Sn(B) correlation in Figure 5n; a roughly linear correlation with gradient 0.88 and $R^2 = 0.63$. While this BE correlation is not as clearly linear as the aforementioned iodine:Sn(II) correlation, when considered alongside the $\%_{at}$ correlation in Figure 5j, discussed above, together these seem strong evidence that the Sn(B) and the O 1s(A) environment are present in the same phase. The $\%_{at}$ correlation showed that the ratio of the Sn to O ratio in this phase is almost exactly 1:1. If the O 1*s*(A) environment, which is around 530 eV in binding energy, is interpreted as an oxide anion, this observed 1:1 ratio suggests a SnO composition. If the Sn(B) component represents Sn (IV) as has been assumed, then other anions must be included in this phase to balance charge. But neither iodide nor the O 1*s*(B) environments seem to be correlated with the Sn(B) phase, as can be seen from the plots in Figure 5. There are three possibilities that we can see: either another unidentified anionic component exists in the same phase as Sn(B), or the assumptions we set out above (constant phase composition, no change in chemical environment over time) are sufficiently false to mean the correlation analysis we use is invalid, or in fact Sn(B) may represent a Sn(II) environment bound to oxygen with 1:1 stoichiometry. This latter case implies that the phase may in fact be tin(II) oxide, SnO. Early reports on SnO / SnO_2 determination by XPS stated that there was no chemical shift in the Sn 3d coreline, and determination should be carried out by quantification of the tin to oxygen ratio.[29, 30] One measure of the BE difference between O 1s and Sn $3d_{5/2}$ in Sn oxides (both SnO_2 and SnO) was 43.9 eV,[30] very close to our difference between O1s (A) and Sn$3d_{5/2}$ (B) of 43.6 eV.

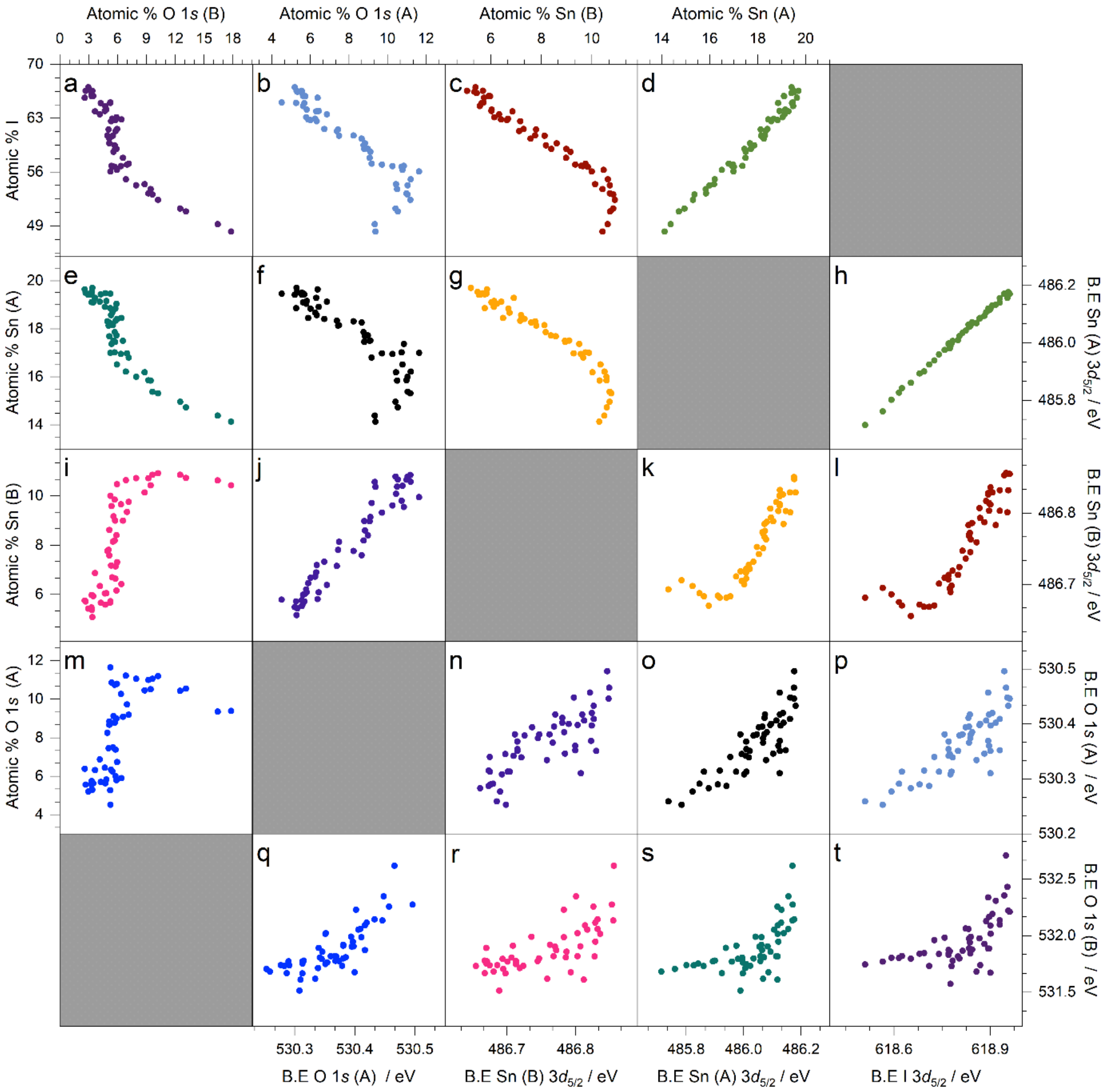

Figure 5. Correlation diagram for XPS of tin perovskite over five chemical environments which are defined in the text: I 3*d*5/2, Sn 3*d*5/2 (A), Sn 3*d*5/2 (B), O 1*s*(A), O 1*s*(B). Top left, atomic% correlations. Bottom right, binding energy correlations.

Considered together, our correlation analysis of the binding energies of principal core lines and components, and the concentrations of the elements and environments they represent across 50 iterations allow us to build a more detailed picture of the surface chemistry than might have been done by consideration of each feature, or iteration, independently. The iodine and Sn(A) core lines correlate strongly in both composition and binding energy. In composition, they have close to the expected 3:1 gradient with almost zero intercept. The former shows the composition is close to 3:1 I:Sn, and the latter shows that there is no Iodine outside of a phase with Sn(A) and vice versa; if it were otherwise the intercept would be non-zero revealing the remainder of one element after the other was totally removed. Likewise, the correlation in the binding energy for the iodine and Sn(A) principal corelines is linear and with a gradient very close to one. This means the shift in each core line is almost identical. Since the peak shape does not change, we rule out any chemical transformation of these peaks, and attribute the BE shift to the changing Fermi level or charging, both of which would act identically on elements in the same phase. We conclude that Sn 3*d*(A) represents Sn(II), and that the level of iodine outside of that phase is very low.

Identification of the Sn(B) environment is more difficult, but it is correlated strongly with the O 1s(A) environment in a 1:1 $\%_{at}$ ratio, leading to the possibility that Sn(B) is in fact Sn(II) oxide, SnO, although other possibilities such as an oxy hydroxide phase or other unidentified anions cannot be ruled out.

Gathering the evidence together, we can conclude the following. Upon air exposure, the surface of the tin perovskite takes up oxygen, and an oxygen and tin rich layer forms at the surface of the material. This layer is unstable under XPS measurement conditions, both X-rays alone and X-ray plus Ar^+ ion flood gun. Over around 50 min of measurement, it decays to result in a surface almost indistinguishable by XPS from the surface present before air exposure.

Conclusions

We have studied tin based halide perovskite thin films by XPS, and specifically addressed the issue of building reliable models for quantification of Sn oxidation state. We have found that the nature of the Sn 3*d* spectrum means that without robust constraints, many seemingly acceptable models can be constructed that may give very different Sn(II) contents. Additionally, exposure of the tin perovskite surface to the measurement conditions, both X-rays alone and X-rays + Ar^+ ion dual beam flood gun, leads to significant chemical changes to the surface. If the analyst is unaware of this instability, it is likely that incorrect measurement of the Sn chemical environment may result.

We use correlation analysis on a dataset of 50 spectra to understand which chemical environments that appear together in phases. We observe a tin – iodide phase with the expected composition, and this supports the validity of our Sn 3*d* modelling, also suggesting that iodine is not present in other phases to a significant extent. The high binding energy Sn 3*d* environment usually attributed to Sn(IV) correlates with an O 1*s* environment in close to a 1:1 ratio. This may indicate this peak originates from a SnO phase, and in this case SnO would be expected to be an oxidation product of the tin perovskite on reaction with air. This particular conclusion rests on the assumptions stated in the correlation analysis which we believe to be suitable for this system but which may be confounded if, for example, the Sn(B) environment originates from more than one phase (e.g. a Sn oxide and a Sn oxyhalide).

We make suggestions for XPS studies of tin perovskite surfaces to help avoid some pitfalls we have identified here:

- Sn(IV) and Sn(II) have closely spaced chemical environments that are usually not resolved. Fitting of the Sn3d to reveal Sn(II)/Sn(IV) ratio requires a well constrained model. **Without it, a wide range of Sn(II)/Sn(IV) ratios can be obtained from a particular spectrum**, making any such conclusions almost meaningless.
- Spectral models should be described in sufficient detail to be reproduced and assessment made of their validity. Constraints should be noted. Fitted component shapes, energies and FWHM should be reported.
- The oxidised tin perovskite surface is unstable under XPS measurement conditions we used (which are common in many XPS measurement systems). The composition of the surface significantly changed over a typical analysis time (1 hour), moving from a highly oxidised surface to one similar to an etched, low oxygen surface. This means if care is not taken, the reported XPS composition may be very strongly influenced by the analytical procedure. If a key finding of the XPS analysis is the oxidation state of the Sn site, sufficient evidence should

be given for stability of the sample in under measurement conditions. This should consist of spectra taken after different lengths of measurement.

- Reporting of only Sn core lines can hide very significant oxidation or non-stoichiometry of the surface. It is best practice to report high resolution core lines for all elements in the compound, as well as a survey spectrum, and O 1*s* and C 1*s* spectra, since these are common surface contaminants.
- Assumption that the higher binding energy Sn 3*d* component is from Sn(IV) may be incorrect, as we show here it may arise from Sn(II) oxide.
- As with all reports, XPS methodology should be explained in sufficient detail. If used, Ar^+ ion etching conditions (mono-Ar, cluster size, energy, etch time) should be reported.

Experimental Methods

Materials

Formamidinium iodide (FAI) and phenethylammonium iodide (PEAI) were purchased from Greatcell Solar. Tin(II) iodide (SnI2, 99.99% with subsequent sublimation treatment), tin(II) fluoride (SnF2, 99%), Cesium carbonate (Sigma, 99%), oleic acid (OA, TCI, 90%), oleylamine (OLA, TCI, 90%), 1-octadecen (ODE, Sigma, 90%), toluene (Thermo Scientific Chemicals, anhydrous, 99.8%) were purchased from Sigma Aldrich. All solvents were purchased from Acros Organics.

Glass substrate preparation

Microscope glass substrates (Fisher) were cut to ≈ 1.3 cm × 1.3 cm and sequentially sonicated in soap solution, deionised water, acetone, and isopropanol alcohol for 15 minutes each. Prior to deposition, the glass slides were surface-treated using ultraviolet-ozone surface treatment for 15 min.

Precursor and film fabrication

The perovskite precursors ($PEA_{0.2}FA_{0.8}Sn(Br_xI_{1-x})_3$, 0.8 M, x = 0, 0.1, 1) were prepared in an N_2 glovebox (0.5ppm>) from PEAI, PEABr, FAI, FABr, SnI_2 and SnF_2 powders in a mixed solvent of 4:1 v/v mixture of DMF and DMSO (both ultradry and bottled with molecular sieves). The solutions were then filtered (0.22 µm, PTFE) and deposited on the substrate via a one-step spin-coating procedure (4000 rpm for 20 s, 700 µl of dry diethyl ether dropped in the middle of the substrate after 9 s elapsed, followed by annealing at 70 °C for 20 min.

Device fabrication

ITO substrates were prepared identically to the glass substrates (vide supra). PEDOT:PSS was then filtered directly onto the substrate (0.45 µm) and spin-coated at 5000 rpm with 2000 rpm acceleration for 30 s under ambient conditions, and subsequently annealed at 140 °C for 20 min. ($PEA_{0.2}FA_{0.8}Sn(Br_xI_{1-x})_3$, 0.8 M, x = 0, 10, 100) were then deposited identically to the perovskite-glass substrates. PCBM (15 mg mL^{-1} in chlorobenzene) was subsequently deposited by spin-coating at 2000 rpm for 30 s, followed by dynamic spin-coating of bathocuproine (BCP,0.5 mg mL^{-1} in IPA) atop the PCBM at 5000 rpm for 20 s. A 100 nm Ag electrode was then deposited via thermal evaporation under a vacuum of 10^{-6} mbar to produce devices with an active area of 0.045 cm^2

Preparation of Cs-oleate precursor

The Cs-oleate precursor was prepared by adding cesium carbonate (0.326 g, 1 mmol), OA (1 ml, 3.2 mmol), and ODE (8 ml) into a 25 ml of 3-necked round bottom flask under stirring. The mixture was vacuumed for 60 mins at 120°C in a Schlenk line, and then heated up to 150°C under N_2 flow until all the powder was dissolved. The Cs-oleate precursor needs to be stored in a N_2 atmosphere and re-heated to 100°C before being used.

Synthesis of $CsSnI_3$ nanocrystals

The tin (II) iodide precursor was prepared by adding tin (II) iodide (0.75 g, 2 mmol), OA (0.63 ml, 2 mmol), OLA (0.66 ml, 2mmol) and ODE (5 ml) into a 25 ml of 3-necked round bottom flask within a N_2 filled glovebox. The chemicals-filled round bottom flask was connected to a Schlenk line and then vacuumed for 10 mins at room temperature under vigorous stirring. The mixture was then heated up to 200°C under N_2 flow until the mixture turned into a clear yellow solution. Subsequently, 2.8 ml of pre-heated Cs-oleate precursor was swiftly injected into the tin (II) iodide precursor. After 10 s, the reaction was quenched by immersing the flask into an ice-bath until the mixture cooled to room temperature.

Purification of $CsSnI_3$ nanocrystals

The crude solution was centrifuged at 8500 rpm for 10 mins to remove the unreacted ligands. The precipitate was redispersed in 10 ml of toluene, followed by a second centrifuging at 8500 rpm for 10 mins. The resulting precipitant was collected and redispersed in 10 ml of toluene.

Deposition of $CsSnI_3$ nanocrystals on glass substrate

A 200 ul of prepared $CsSnI_3$ nanocrystals solution was drop-cast onto a clean glass substrate.

XPS Analysis

X-ray photoelectron spectroscopy (XPS) was carried out in a Thermo NEXSA spectrometer. The instrument utilized a 72W monochromated Al Kα X-ray source ($E = 1486.6$ eV) focused to a spot of 400 μm diameter at the sample surface. Charge compensation was accomplished by use of a dual beam (electron and Ar^+ ion) flood gun. The electron energy analyser consisted of a double focusing 180° hemisphere with mean radius 125 mm, operated in constant analyser energy (CAE) mode, and a 128 channel position sensitive detector. The pass energy was set to 200 eV for survey scans and 40 eV for high resolution regions. The binding energy scale of the instrument is regularly calibrated using a three-point energy reference (Ag, Au, Cu).

Acknowledgements

X-ray photoelectron data collection was performed at the EPSRC National XPS Service, grant number EP/Y023587/1

References

1. Béchu, S.; Ralaiarisoa, M.; Etcheberry, A.; Schulz, P., Photoemission Spectroscopy Characterization of Halide Perovskites. **2020,** *10* (26), 1904007.
2. Sharif, R.; Khalid, A.; Ahmad, S. W.; Rehman, A.; Qutab, H. G.; Akhtar, H. H.; Mahmood, K.; Afzal, S.; Saleem, F., A comprehensive review of the current progresses and material advances in perovskite solar cells. *Nanoscale Advances* **2023,** *5* (15), 3803-3833.
3. Aktas, E.; Rajamanickam, N.; Pascual, J.; Hu, S.; Aldamasy, M. H.; Di Girolamo, D.; Li, W.; Nasti, G.; Martínez-Ferrero, E.; Wakamiya, A.; Palomares, E.; Abate, A., Challenges and strategies

toward long-term stability of lead-free tin-based perovskite solar cells. *Communications Materials* **2022,** *3* (1), 104.

4. Cao, J.; Yan, F., Recent progress in tin-based perovskite solar cells. *Energy & Environmental Science* **2021,** *14* (3), 1286-1325.

5. Lanzetta, L.; Webb, T.; Marin-Beloqui, J. M.; Macdonald, T. J.; Haque, S. A., Halide Chemistry in Tin Perovskite Optoelectronics: Bottlenecks and Opportunities. *Angewandte Chemie (International ed. in English)* **2023,** *62* (8), e202213966.

6. Lanzetta, L.; Webb, T.; Zibouche, N.; Liang, X.; Ding, D.; Min, G.; Westbrook, R. J. E.; Gaggio, B.; Macdonald, T. J.; Islam, M. S.; Haque, S. A., Degradation mechanism of hybrid tin-based perovskite solar cells and the critical role of tin (IV) iodide. *Nature Communications* **2021,** *12* (1), 2853.

7. Kurisinkal Pious, J.; Zwirner, Y.; Lai, H.; Olthof, S.; Jeangros, Q.; Gilshtein, E.; Kothandaraman, R. K.; Artuk, K.; Wechsler, P.; Chen, C.; Wolff, C. M.; Zhao, D.; Tiwari, A. N.; Fu, F., Revealing the Role of Tin Fluoride Additive in Narrow Bandgap Pb-Sn Perovskites for Highly Efficient Flexible All-Perovskite Tandem Cells. *ACS Applied Materials & Interfaces* **2023,** *15* (7), 10150-10157.

8. Joy, S.; Atapattu, H. R.; Sorensen, S.; Pruett, H.; Olivelli, A. B.; Huckaba, A. J.; Miller, A.-F.; Graham, K. R., How additives for tin halide perovskites influence the Sn4+ concentration. *Journal of Materials Chemistry A* **2022,** *10* (25), 13278-13285.

9. Karim, M. A.; Matsuishi, K.; Chowdhury, T. H.; Abdel-Shakour, M.; He, Y.; Islam, A., Additive-Assisted Electronic Defect Passivation in Lead-Free Tin Perovskite Solar Cells: Suppression of Sn2+ Oxidation and I– Losses. *ACS Applied Energy Materials* **2022,** *5* (12), 15038-15047.

10. Zhang, Z.; Wang, L.; Kumar Baranwal, A.; Razey Sahamir, S.; Kapil, G.; Sanehira, Y.; Akmal Kamarudin, M.; Nishimura, K.; Ding, C.; Liu, D.; Li, Y.; Li, H.; Chen, M.; Shen, Q.; Ripolles, T. S.; Bisquert, J.; Hayase, S., Enhanced efficiency and stability in Sn-based perovskite solar cells by trimethylsilyl halide surface passivation. *Journal of Energy Chemistry* **2022,** *71*, 604-611.

11. Bagus, P. S.; Nelin, C. J.; Brundle, C. R., Chemical significance of x-ray photoelectron spectroscopy binding energy shifts: A Perspective. *Journal of Vacuum Science & Technology A* **2023,** *41* (6).

12. Stranick, M. A.; Moskwa, A., SnO2 by XPS. *Surface Science Spectra* **1993,** *2* (1), 50-54.

13. Wieczorek, A.; Lai, H.; Pious, J.; Fu, F.; Siol, S., Resolving Oxidation States and X–site Composition of Sn Perovskites through Auger Parameter Analysis in XPS. **2023,** *10* (7), 2201828.

14. Cruz, M.; Morales, J.; Espinos, J. P.; Sanz, J., XRD, XPS and 119Sn NMR study of tin sulfides obtained by using chemical vapor transport methods. *Journal of Solid State Chemistry* **2003,** *175* (2), 359-365.

15. Wang, L.; Miao, Q.; Wang, D.; Chen, M.; Bi, H.; Liu, J.; Baranwal, A. K.; Kapil, G.; Sanehira, Y.; Kitamura, T.; Ma, T.; Zhang, Z.; Shen, Q.; Hayase, S., 14.31 % Power Conversion Efficiency of Sn-Based Perovskite Solar Cells via Efficient Reduction of Sn4+. **2023,** *62* (33), e202307228.

16. Li, C.; Zhang, N.; Gao, P., Lessons learned: how to report XPS data incorrectly about lead-halide perovskites. *Materials Chemistry Frontiers* **2023,** *7* (18), 3797-3802.

17. Cazaux, J., Mechanisms of charging in electron spectroscopy. *Journal of Electron Spectroscopy and Related Phenomena* **1999,** *105* (2), 155-185.

18. Baer, D. R.; Artyushkova, K.; Cohen, H.; Easton, C. D.; Engelhard, M.; Gengenbach, T. R.; Greczynski, G.; Mack, P.; Morgan, D. J.; Roberts, A., XPS guide: Charge neutralization and binding energy referencing for insulating samples. *Journal of Vacuum Science & Technology A* **2020,** *38* (3).

19. Greczynski, G.; Hultman, L., X-ray photoelectron spectroscopy: Towards reliable binding energy referencing. *Progress in Materials Science* **2020,** *107*, 100591.

20. Su, Y.; Yang, J.; Liu, G.; Sheng, W.; Zhang, J.; Zhong, Y.; Tan, L.; Chen, Y., Acetic Acid-Assisted Synergistic Modulation of Crystallization Kinetics and Inhibition of Sn 2+ Oxidation in Tin-Based Perovskite Solar Cells. *Advanced Functional Materials* **2021,** *32*, 2109631.

21. Abbasli, M.; Hieulle, J.; Schrage, J.; Wilks, D.; Samad, A.; Schwingenschlögl, U.; Redinger, A.; Busse, C.; Ohmann, R., Tin Halide Perovskite Epitaxial Films on Gold Surfaces: Atomic Structure and Stability. *n/a* (n/a), 2403680.

22. Bagus, P. S.; Ilton, E.; Nelin, C. J., Extracting Chemical Information from XPS Spectra: A Perspective. *Catalysis Letters* **2018,** *148* (7), 1785-1802.

23. Briggs, D.; Beamson, G., XPS studies of the oxygen 1s and 2s levels in a wide range of functional polymers. *Analytical Chemistry* **1993,** *65* (11), 1517-1523.

24. Kim, J.; Park, J.-S.; Kim, G. Y.; Jo, W., Autonomous Control of Ion Migration at α-FAPbI3 Heterointerfaces via Interfacial-Self-Assembled 2D Perovskite. *n/a* (n/a), 2402117.

25. Juarez-Perez, E. J.; Ono, L. K.; Qi, Y., Thermal degradation of formamidinium based lead halide perovskites into sym-triazine and hydrogen cyanide observed by coupled thermogravimetry-mass spectrometry analysis. *Journal of Materials Chemistry A* **2019,** *7* (28), 16912-16919.

26. Lin, W.-C.; Lo, W.-C.; Li, J.-X.; Wang, Y.-K.; Tang, J.-F.; Fong, Z.-Y., In situ XPS investigation of the X-ray-triggered decomposition of perovskites in ultrahigh vacuum condition. *npj Materials Degradation* **2021,** *5* (1), 13.

27. Gupta, S.; Bendikov, T.; Hodes, G.; Cahen, D., CsSnBr3, A Lead-Free Halide Perovskite for Long-Term Solar Cell Application: Insights on SnF2 Addition. *ACS Energy Letters* **2016,** *1* (5), 1028-1033.

28. Bhatt, P.; Isaacs, M.; Liu, Y.; Palgrave, R. G., Correlation analysis in X-ray photoemission spectroscopy. *Applied Surface Science* **2024,** *672*, 160808.

29. Dobler, D.; Oswald, S.; Wetzig, K., Calibration of XPS – energy scale for determination of the oxidation states of doping elements in SnO2 powders. *Analytical and Bioanalytical Chemistry* **2002,** *374* (4), 646-649.

30. Lau, C. L.; Wertheim, G. K., Oxidation of tin: An ESCA study. *Journal of Vacuum Science and Technology* **1978,** *15* (2), 622-624.